International Journal of Mechanical Sciences 178 (2020) 105609

Contents lists available at ScienceDirect

International Journal of Mechanical Sciences

journal homepage: www.elsevier.com/locate/ijmecsci

Thermo-hydrodynamic and entropy generation analysis of a dilute aqueous suspension enhanced with nano-encapsulated phase change material

Seyed Mohsen Hashem Zadeh[a], S.A.M. Mehryan[b], Mikhail Sheremet[c], Maryam Ghodrat[d], Mohammad Ghalambaz[e,f,*]

[a] Department of Mechanical Engineering, Shahid Chamran University of Ahvaz, Iran
[b] Young Researchers and Elite Club, Yasooj Branch, Islamic Azad University, Yasooj, Iran
[c] Laboratory on Convective Heat and Mass Transfer, Tomsk State University, Tomsk, Russia
[d] School of Engineering and Information Technology, University of New South Wales Canberra, Canberra 2610 ACT, Australia
[e] Metamaterials for Mechanical, Biomechanical and Multiphysical Applications Research Group, Ton Duc Thang University, Ho Chi Minh City, Vietnam
[f] Faculty of Applied Sciences, Ton Duc Thang University, Ho Chi Minh City, Vietnam

ARTICLE INFO

Keywords:
Conjugate natural convection
Entropy generation
Fusion temperature
Nano-encapsulated phase change material
Solid triangular block

ABSTRACT

The present study is devoted to the numerical analysis of entropy generation in the natural convection of water combined with nano-sized particles containing the encapsulated phase change material in a square enclosure with a solid triangular block. The finite element method is used for the current investigation. The effects of the Rayleigh (Ra), Stefan numbers (Ste), thermal conductivity ratio (R_k) and non-dimensional height (L_Y) of the triangular block, the volume fraction (φ), and the non-dimensional fusion temperature (θ_f) of the nano-encapsulated phase change materials are reported. The results show that the rate of heat transfer and the total entropy generation enhances with the increment of the thermal conductivity of the solid triangular block and also declines with augmentation of its height. Moreover, the generated entropy intensifies as the volume fraction of the nano-capsules increases. Finally, for high values of the Rayleigh number ($Ra = 10^6$), the total entropy generation declines as the non-dimensional fusion temperature (θ_f) approaches 0.5. In contrast, when the buoyancy force is low ($Ra = 10^4$), the total generated entropy elevates as $\theta_f \to 0.5$.

1. Introduction

Creation of modern heat exchangers, solar collectors, energy storage systems demands the usage of materials with high heat capacity and latent energy. Phase change materials (PCMs) can be considered as an effective medium having such characteristics [1–3]. Moreover, a phase change for such materials occurs at a constant temperature. An application of PCMs in different devices is related to an opportunity of having an optimal inclusion of these materials within the heat transfer liquid. Such inclusion can be implemented through an encapsulation technique [4,5]. This approach allows keeping PCM in a restricted space and eliminating interaction between PCM and the heat transfer liquid. Thus, Huo et al. [6] considered a prospect of using micro-encapsulated phase change materials with urea-formaldehyde resin shell in order to control the heat transfer performance and temperature distributions within the cement slurry system. These authors showed that the inclusion of the micro-encapsulated phase change materials allows declining both the temperature growth and the hydration heat of the considered system.

Experimental analysis of the cooling performance of three different PCMs in a plate heat exchanger was conducted by Kumirai et al. [7]. They revealed that paraffinic PCMs have great momentary heat absorption with a low absorption period, while salt hydrate PCMs have a longer energy absorption period, but the momentary energy absorption capacity is low. Bhagat and Saha [8] numerically studied the heat transfer performance within a cylinder filled with spherical encapsulated phase change material. Ansys FLUENT commercial software was used for computations. The authors showed that decreasing the encapsulation size leads to diminishing the fluctuation in heat transfer fluid temperature. Li and Chen [9] examined an application of PCM in a building envelope to reduce building heat consumption and improve the heat comfort within the room. The authors considered the bounded porous wall filled with encapsulated PCMs. Numerical analysis was performed using COMSOL Multiphysics software. It was ascertained that the influence of the PCM spheres size on heat transfer performance is non-essential. Moreover, they found that the thickness of the considered wall should be between 6 and 8 cm.

* Corresponding author
E-mail addresses: mohsen.hashemzadeh@gmail.com (S. Hashem Zadeh), alal171366244@gmail.com (S.A.M. Mehryan), sheremet@math.tsu.ru (M. Sheremet), m.ghodrat@adfa.edu.au (M. Ghodrat), mohammad.ghalambaz@tdtu.edu (M. Ghalambaz).

https://doi.org/10.1016/j.ijmecsci.2020.105609
Received 7 February 2020; Received in revised form 5 March 2020; Accepted 10 March 2020
Available online 11 March 2020

Numerical and experimental analysis of heat transfer in a cylindrical cavity filled with PCM or aluminum foam with PCM was conducted by Caliano et al. [10]. Experiments were performed in a climatic chamber, while numerical analysis was conducted based on the COMSOL Multiphysics software. The authors showed that the addition of aluminum foam allows reducing the charging and recharging periods for PCM in comparison with pure PCM.

There are some published papers about the usage of nano-encapsulated phase change material on different devices. Praveen et al. [11] experimentally analyzed the heat transfer in finned energy storage saturated with graphene nano-platelets with microencapsulated PCM. The authors found that the addition of nano-encapsulated phase change material allows delaying the heat sink temperature growth by 22.5% up to a temperature of 80 °C. Rao et al. [12] considered the heat and mass transport of NEPCM using *n*-octadecane as a core medium and SiO_2 as a shell medium. Molecular dynamics techniques were used for numerical analysis. Authors showed that the shell thickness has an essential impact on the heat transfer performance.

Ghalambaz et al. [13,14] and Hajjar et al. [15] studied the heat transfer of NEPCM in different regions, namely, vertical flat plate [13] and square cavity [14,15]. The authors revealed the energy transport enhancement by using encapsulated PCM nano-sized particles. Li et al. [16] experimentally evaluated the passive thermal efficiency of a metal foam saturated with a slurry containing nano-encapsulated phase change materials. They showed that due to the fluid flow resistance caused by the porosity of the metal foam, the natural convection could vanish entirely. They also reported that the surface temperature was reduced by 24% for the case of pure NEPCMs, while the maximum achievable temperature reduction for the case of metal foam and NEPCMs is about 38%. Tumirah et al. [17] fabricated an organic phase change material of n-octadecane and showed that the prepared NEPCMs have good thermal reliability concerning chemical reactions, showing their potential for thermal energy storage in buildings and other applications.

The entropy generation of nanofluids, containing solid nanoparticles with no phase change, has been investigated in several recent studies. Rashidi et al. [18] investigated the entropy generation of alumina nanofluids in a solar still and found that using a 5% volume fraction of the nanoparticles improves the still production by 25%. Also, the thermal and the friction entropy generations were promoted by using nanoparticles. They also found that thermal entropy generation was the dominant source of the entropy generation in the solar still. Sheikholeslami et al. [19] explored the free convection entropy generation of titania (TiO2), silver (Ag), copper (Cu), and alumina (Al2O3) nanoparticles suspended in water and showed that the presence of nanoparticles raised the overall entropy generation in a cavity. Moreover, the silver nanoparticles resulted in the maximum heat transfer and entropy generation.

Sheremet et al. [20] examined the entropy generation of nanofluids in a cavity containing a hot solid block and reported an increase of entropy generation by the growth of nanoparticles volume fraction. The literature review shows that various aspects of entropy generation of nanofluids such as natural convection in open [21] or partitioned [22] cavities, mixed convection heat transfer [23–25], natural convection of nanofluids in porous media [26], conjugate heat transfer [27], magnetic field effects [28,29], and hybrid nanofluids [29,30] were investigated in recent studies. However, the entropy generation of nano-encapsulated phase change suspensions is a new topic, which has not been addressed yet.

A detailed survey of existing literature reveals that in spite of several studies performed in the domain of thermal analysis of nano-encapsulated phase change materials, the configurational impact of a solid block on the melting zone of the NEPCMs, and how it affects the pattern and rate of heat transfer has not yet analyzed.

In addition, to the best of the author's knowledge, the entropy generation and its dependency on the presence of the NEPCM nanoparticles have not been surveyed in the literature. The present study aims to investigate the fluid flow, heat transfer, and entropy generation in a differentially-heated square cavity filled with water containing nano-encapsulated phase change material under the impact of a heat-conducting solid triangular block. In fact, the aim of using the heat-conducting block with triangular configuration is to study the directional effects of the heat conduction on the flow and heat transfer characteristics, especially the melting-solidification zone. For this purpose, and in order to make the results comparable, the surface area of the triangle is considered to be constant, i.e., the length of the triangular block decreases as its height augments.

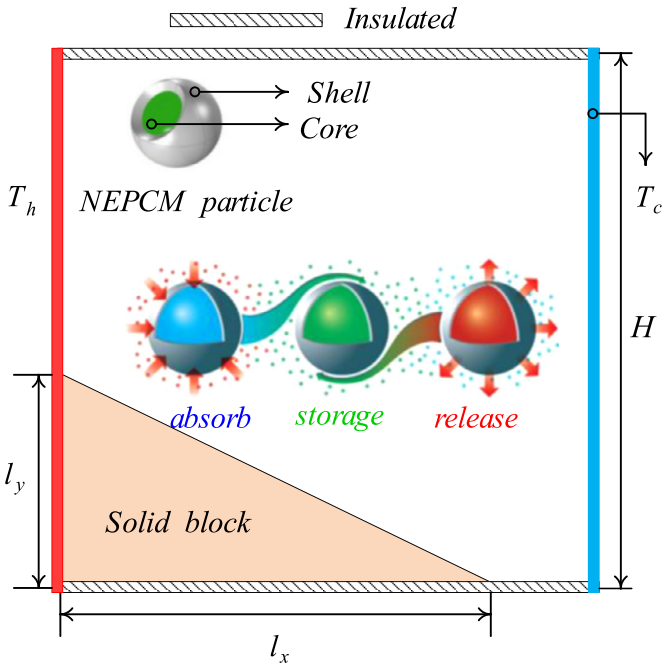

Fig. 1. Schematic figure of the problem physics.

2. Problem physics

The analyzed geometry considered in this study is a 2-dimensional in space cavity with an attached solid triangular block as schematically depicted in Fig. 1. The left and right walls are assumed to be isothermally heated at T_h and T_c, respectively, and the other walls of the enclosure are well insulated. The area of the solid triangular block is constant and is considered as a constraint. The void space of the enclosure is occupied with a suspension of water and the particles of NEPCMs, which circulates by natural convection. The thermophysical properties of the host fluid (water), the core (nonadecane) and the shell (polyurethane) are shown in Table 1. According to the literature [31], the latent heat of the nonadecane is about 211 kJ/kg, and its fusion temperature is approximately 32 °C. The suspension is considered to be homogenous, and no hydrodynamic or thermal slip is assumed. Considering the Boussinesq's approximation to model the variations of the density for the buoyancy force for the laminar, incompressible and steady flow, the thermal and hydrodynamic behaviors of the suspension containing NEPCMs can be expressed as:

$$\frac{\partial u}{\partial x}+\frac{\partial v}{\partial y}=0 \tag{1}$$

$$\rho_b\left(u\frac{\partial u}{\partial x}+v\frac{\partial u}{\partial y}\right)=-\frac{\partial p}{\partial x}+\mu_b\left(\frac{\partial^2 u}{\partial x^2}+\frac{\partial^2 u}{\partial y^2}\right) \tag{2}$$

$$\rho_b\left(u\frac{\partial v}{\partial x}+v\frac{\partial v}{\partial y}\right)=-\frac{\partial p}{\partial y}+\mu_b\left(\frac{\partial^2 v}{\partial x^2}+\frac{\partial^2 v}{\partial y^2}\right)+g\rho_b\beta_b(T-T_c) \tag{3}$$

Table 1
Thermophysical characteristics of the studied materials [31,32].

Material	k (W/m.K)	ρ (kg/m^3)	C_p (J/kg.K)	β (K^{-1})	μ (kg/m.s)
Host fluid (water)	0.613	997.1	4179	21×10^{-5}	8.9×10^{-4}
Polyurethane	–	786	1317.7	17.28×10^{-5}	–
Nonadecane	–	721	2037	–	–
Glass balls	1.05	2700	840	0.9×10^{-5}	–

Table 2
Grid independency test for the Nu_t and the $|\psi_{max}|$.

Case no.	Total number of elements	Nu_t	Err (%)	$\lvert\psi_{max}\rvert$	Err (%)
1	2485	12.9896	0.0438	28.7266	0.2545
2	3662	13.0015	0.0477	28.7586	0.1434
3	5520	12.9953	–	28.7999	–
4	7172	13.0041	0.0677	28.8146	0.0510
5	11,141	13.0039	0.0661	28.8178	0.0621

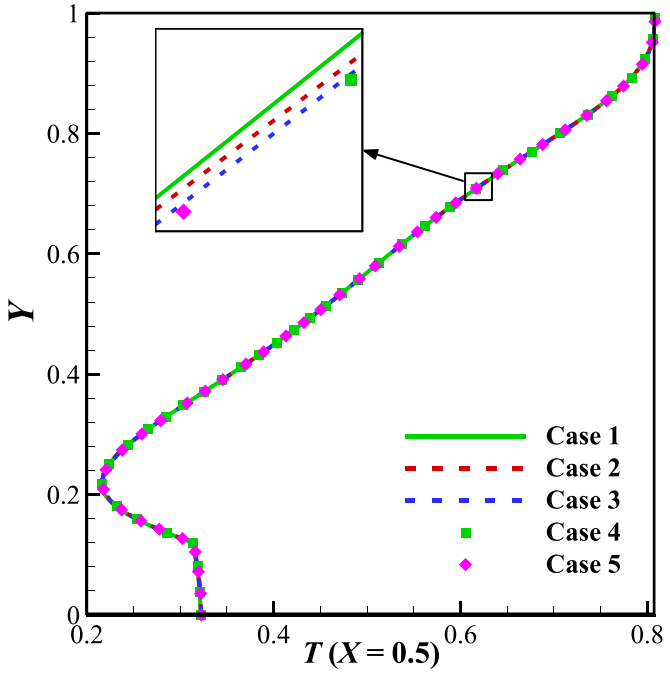

Fig. 2. Temperature profile of the suspension along the vertical centerline of the cavity for different grid resolution ($X = 0.5$).

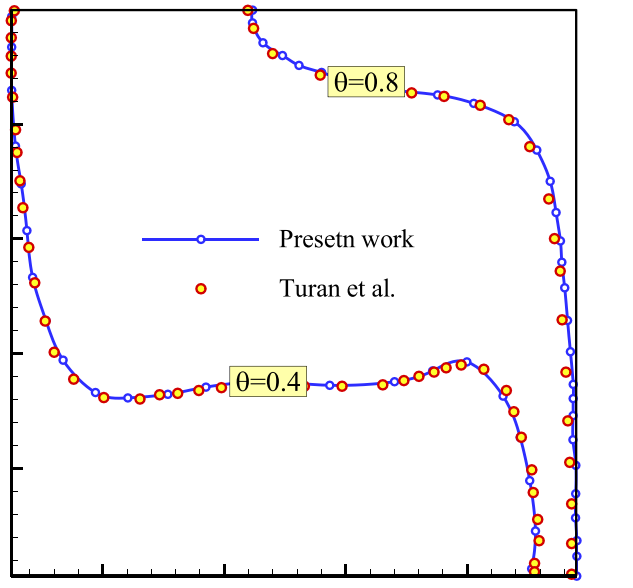

Fig. 3. The temperature field obtained by the current code and represented by Turan et al. [42].

$$\left(\rho C_p\right)_b\left(u\frac{\partial T}{\partial x}+v\frac{\partial T}{\partial y}\right)=k_b\left(\frac{\partial^2 T}{\partial x^2}+\frac{\partial^2 T}{\partial y^2}\right) \tag{4}$$

$$k_s\left(\frac{\partial^2 T}{\partial x^2}+\frac{\partial^2 T}{\partial y^2}\right)=0 \tag{5}$$

Mathematical representation of the boundary conditions is:

$$\forall\, x,y \;|\; \begin{matrix} x=0,\ 0\le y\le l_y \ \Rightarrow T=T_h \\ x=0,\ l_y\le y\le H \Rightarrow u=v=0,\ T=T_h \end{matrix} \tag{6a}$$

$$\forall\, x,y \;|\; x=H,\ 0\le y\le H \ \Rightarrow u=v=0,\ T=T_c \tag{6b}$$

$$\forall\, x,y \;|\; \begin{matrix} y=0,\ 0\le x\le l_x \Rightarrow \partial T/\partial y=0 \\ y=0,\ l_x\le x\le H \Rightarrow u=v=0\ ,\partial T/\partial y=0 \end{matrix} \tag{6c}$$

$$\forall\, x,y \;|\; y=H,\ 0\le x\le H \Rightarrow u=v=0\ ,\ \partial T/\partial y=0 \tag{6d}$$

$$\forall\, x,y \;\Big|\; y=-\left(l_y/l_x\right)\left(x-l_x\right) \Rightarrow u=v=0\ ,\ k_s\left.\frac{\partial T}{\partial n}\right|_s=k_b\left.\frac{\partial T}{\partial n}\right|_b \tag{6e}$$

2.1. The suspension thermo-physical properties

The suspension density is defined and assessed as a weighted function of the base fluid and the dispersed nano-particles [33]:

$$\rho_b=(1-\varphi)\rho_f+\varphi\rho_p \tag{7}$$

The subscripts p and f respectively represent the particles and host fluid. The density of the NEPCMs can be calculated as following [33,34]:

$$\rho_p=\frac{(1+\iota)\rho_{co}\rho_{sh}}{\rho_{sh}+\iota\rho_{co}} \tag{8}$$

The subscripts sh and co denote the densities of the shell and core of NEPCMs, respectively. ι, which is the weight ratio of the core to the shell and for the studied materials, approximately equals $\iota \approx 0.447$ [31]. Also, the suspension's heat capacity is calculated as follows [34,35]:

$$C_{p,b}=\frac{(1-\varphi)\rho_f C_{p,f}+\varphi\rho_p C_{p,p}}{\rho_b} \tag{9}$$

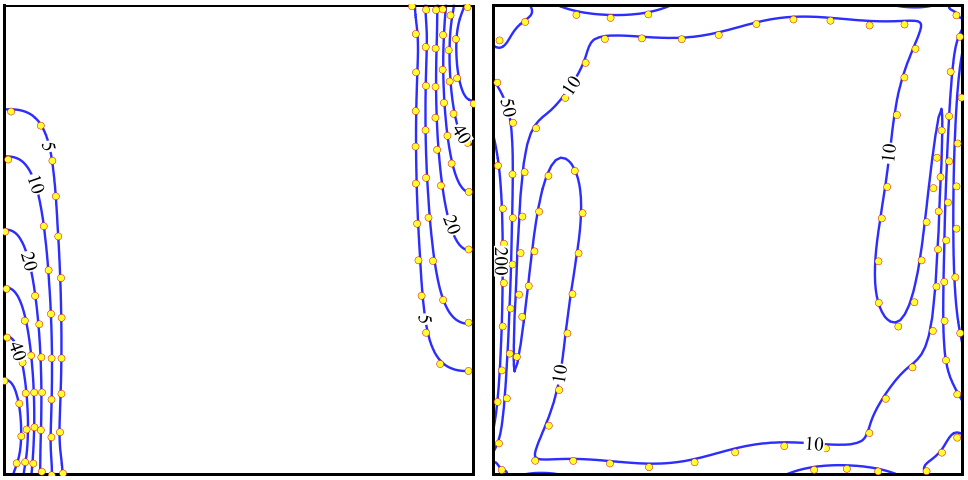

Fig. 4. Entropy generation induced by (left) thermal gradient and (right) viscosity for the present work (solid lines) and Ilis et al. [43] (circle symbol).

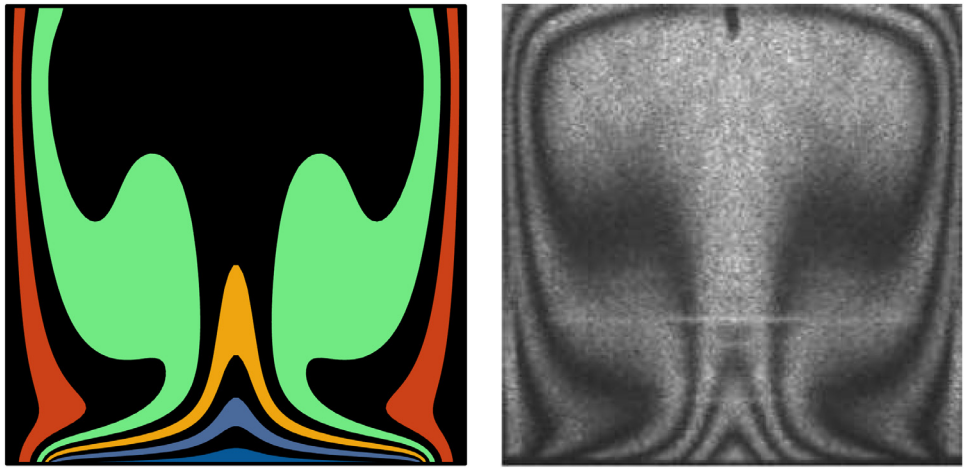

Fig. 5. A comparison between the isotherms of (a): the present numerical work and (b): the experimental work conducted by Calcagni et al. [44].

With regard to the phase transition of the core of the nano-capsules, the following sinusoidal profile is suggested for the total heat capacity [33,36]:

$$C_{p,p} = C_{p,co} + \left\{ \frac{\pi}{2} \cdot \left(\frac{h_{sf}}{T_{Mr}} - C_{p,co} \right) \cdot \sin\left(\pi \frac{T - T_0}{T_{Mr}} \right) \right\} \times \begin{cases} 0 & T < T_0 \\ 1 & T_0 < T < T_1 \\ 0 & T > T_1 \end{cases} \tag{10}$$

in which T_{Mr}, the temperature interval, is defined as:

$$T_{Mr} = T_1 - T_0 \left| \begin{array}{l} T_0 = T_f - T_{Mr}/2 \\ T_1 = T_f + T_{Mr}/2 \end{array} \right. \tag{11}$$

T_f is the fusion temperature of the core. The phase change occurs in the cores of the nano-capsules, where the temperature of the suspension varies between T_0 and T_1. The volumetric thermal expansion coefficient of the suspension can be expressed as [35]:

$$\beta_b = (1 - \varphi)\beta_f + \varphi\beta_p \tag{12}$$

The dynamic viscosity and thermal conductivity of the suspension are evaluated by utilizing the linear relations presented below [37,38]:

$$\frac{\mu_b}{\mu_f} = 1 + Nv\varphi \tag{13a}$$

$$\frac{k_b}{k_f} = 1 + Nc\varphi \tag{13b}$$

where the Nc and Nv are respectively the numbers of dynamic viscosity and thermal conductivity. It is worth noting that the Eq. (13) can be employed only when $\varphi \leq 5\%$. Using curve-fitting on the experimental research of Barlak et al. [31], the values of $Nc = 23.8$ and $Nv = 12.5$ are computed for NEPCMs in water. The NEPCM particles were made of n-Nonadecane core and polyurethane shell.

2.2. Stream function and entropy generation

Suspension flow can be visualized by employing the contours of the stream function, defined by the velocity components as follows:

$$u = \frac{\partial \psi}{\partial y}, v = -\frac{\partial \psi}{\partial x} \tag{14}$$

Once again, differentiating the above equations with respect to x and y, and then, subtracting the resulted equations yields:

$$\frac{\partial^2 \psi}{\partial x^2} + \frac{\partial^2 \psi}{\partial y^2} = -\left(\frac{\partial v}{\partial x} - \frac{\partial u}{\partial y} \right) \tag{15}$$

The required boundary conditions for the above equation are $\psi = 0$ overall the bounds.

The following equation shows the mechanism for the production of entropy including thermal entropy generation and friction entropy

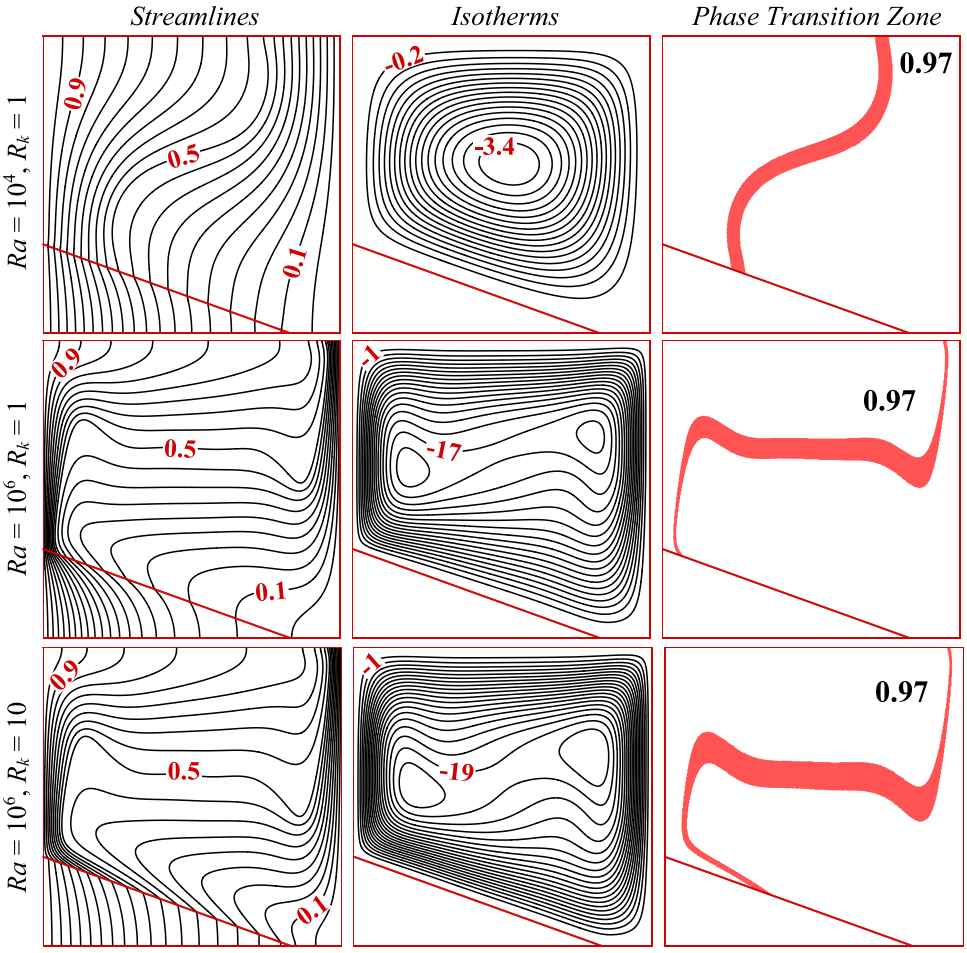

Fig. 6. Influence of the Rayleigh number and the R_k on the patterns of the isotherms, streamlines and the phase transition zone ($\varphi = 0.05$, $Ste = 0.2$, $\theta_f = 0.5$, $L_Y = 0.3$).

generation [39] as

$$s = s_\theta + s_\psi = \frac{k_b}{T_0^2}\left[\left(\frac{\partial T}{\partial x}\right)^2 + \left(\frac{\partial T}{\partial y}\right)^2\right] + \frac{\mu_b}{T_0}\left(2\left(\left(\frac{\partial u}{\partial x}\right)^2 + \left(\frac{\partial v}{\partial y}\right)^2\right) + \left(\frac{\partial u}{\partial y} + \frac{\partial v}{\partial x}\right)^2\right) \tag{16}$$

where s_θ and s_ψ in the above equation refer to the entropy generations because of temperature gradient and friction of the fluid layers, respectively.

3. Non-dimensionalizing the governing equations

To normalize the Eqs. (1–4) along with the assumed boundary conditions, i.e., Eq. (5), the following definition is employed:

$$X = \frac{x}{H},\ Y = \frac{y}{H},\ U = \frac{uH}{\alpha_f},\ V = \frac{vH}{\alpha_f},\ \Psi = \frac{\psi}{\alpha_f},\ P = \frac{pH^2}{\rho_f \alpha_f^2}$$
$$\theta = \frac{T - T_c}{\Delta T},\ \Pi = \frac{\pi}{k_f \Delta T},\ \Delta T = T_h - T_c \tag{17}$$

Hence, we then have:

$$\frac{\partial U}{\partial X} + \frac{\partial V}{\partial Y} = 0 \tag{18}$$

$$\left(\frac{\rho_b}{\rho_f}\right)\left(U\frac{\partial U}{\partial X} + V\frac{\partial U}{\partial Y}\right) = -\frac{\partial P}{\partial X} + Pr\left(\frac{\mu_b}{\mu_f}\right)\left(\frac{\partial^2 U}{\partial X^2} + \frac{\partial^2 U}{\partial Y^2}\right) \tag{19}$$

$$\left(\frac{\rho_b}{\rho_f}\right)\left(U\frac{\partial V}{\partial X} + V\frac{\partial V}{\partial Y}\right) = -\frac{\partial P}{\partial Y} + Pr\left(\frac{\mu_b}{\mu_f}\right)\left(\frac{\partial^2 V}{\partial X^2} + \frac{\partial^2 V}{\partial Y^2}\right) + Ra \cdot Pr\left(\frac{\rho_b}{\rho_f}\right)\left(\frac{\beta_b}{\beta_f}\right)\theta \tag{20}$$

in the above equations, the Rayleigh (Ra) and the Prandtl (Pr) numbers, are:

$$Ra = \frac{g\rho_f \beta_f \Delta T H^3}{\alpha_f \mu_f},\ Pr = \frac{\mu_f}{\rho_f \alpha_f} \tag{21}$$

$$Cr\left(U\frac{\partial \theta}{\partial X} + V\frac{\partial \theta}{\partial Y}\right) = \left(\frac{k_b}{k_f}\right)\left(\frac{\partial^2 \theta}{\partial X^2} + \frac{\partial^2 \theta}{\partial Y^2}\right) \tag{22}$$

where

$$Cr = \frac{(\rho C_p)_b}{(\rho C_p)_f} = (1-\varphi) + \varphi\lambda + \frac{\varphi}{\delta\, Ste} f \tag{23}$$

Cr is the heat capacity of the suspension divided by the sensible heat capacity of the host fluid. Also, the heat capacity ratio λ, the dimensionless melting interval δ, and the Stefan number Ste are defined as:

$$\lambda = \frac{(Cp_{c,l} + \imath Cp_s)\rho_c \rho_s}{(\rho Cp)_f(\rho_s + \imath\rho_c)},\ \delta = \frac{T_{Mr}}{\Delta T},\ Ste = \frac{(\rho Cp)_f \Delta T(\rho_s + \imath\rho_c)}{\alpha_f(h_{sf}\rho_c\rho_s)} \tag{24}$$

Also, f, the dimensionless fusion function, is defined as:

$$f = \frac{\pi}{2}\sin\left(\frac{\pi}{\delta}\left(\theta - \theta_f + \frac{\delta}{2}\right)\right) \times \begin{cases} 0 & \theta < \theta_f - \delta/2 \\ 1 & \theta_f - \delta/2 < \theta < \theta_f + \delta/2 \\ 0 & \theta > \theta_f + \delta/2 \end{cases} \tag{25}$$

Where θ_f, the dimensionless fusion temperature, is.

$$\theta_f = \frac{T_f - T_c}{\Delta T} \tag{26}$$

The energy equation for the solid triangular block is:

$$0 = R_k\left(\frac{\partial^2 \theta}{\partial X^2} + \frac{\partial^2 \theta}{\partial Y^2}\right) \Big| \ R_k = \frac{k_s}{k_b} \tag{27}$$

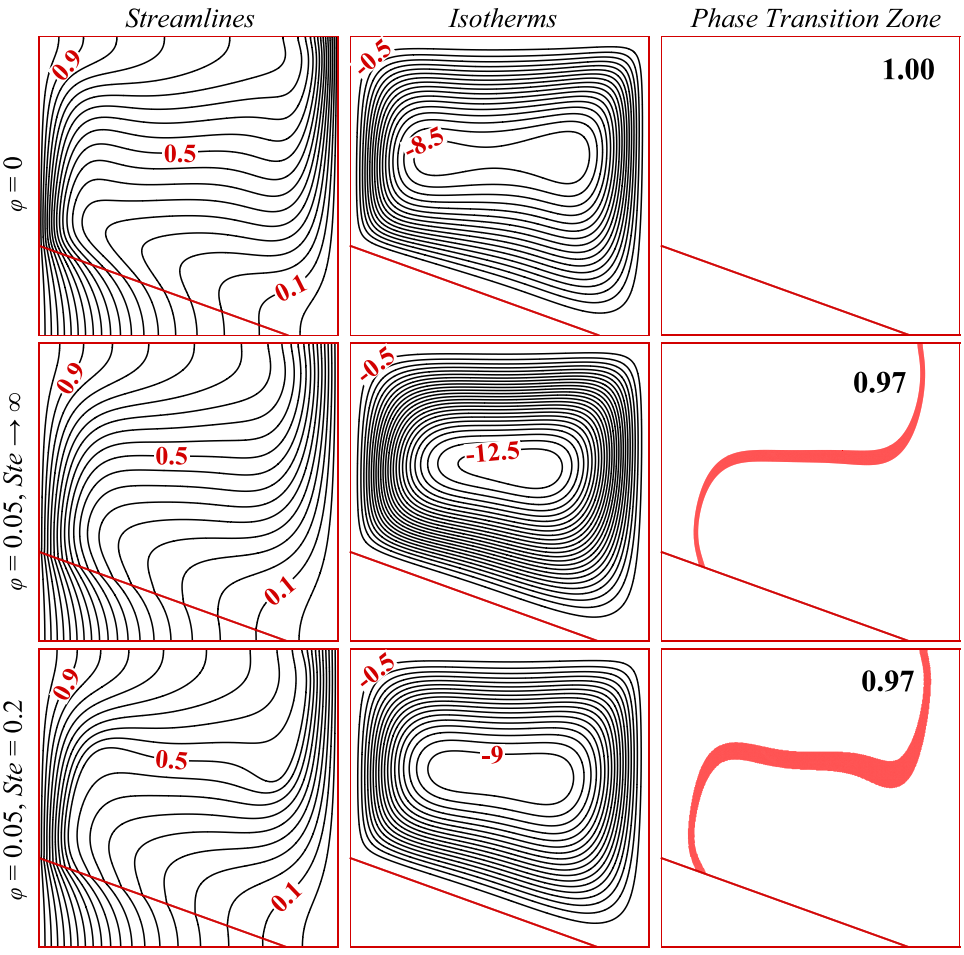

Fig. 7. Influence of the volume fraction of the NEPCMs and the Stefan number on the patterns of the isotherms, streamlines and the phase transition zone ($Ra = 10^5$, $R_k = 1$, $\theta_f = 0.5$, $L_Y = 0.3$).

The non-dimensional form of the imposed boundary conditions can be expressed as:

$$\forall\, X,Y \mid \begin{array}{l} X=0,\ 0\le Y\le L_Y \ \Rightarrow \theta=1 \\ X=0,\ L_Y\le Y\le 1 \Rightarrow U=V=0,\ \theta=1 \end{array} \tag{28a}$$

$$\forall\, X,Y \mid X=1,\ 0\le Y\le 1 \ \Rightarrow U=V=0,\ \theta=0 \tag{28b}$$

$$\forall\, X,Y \mid \begin{array}{l} Y=0,\ 0\le X\le L_X \Rightarrow \partial\theta/\partial Y=0 \\ Y=0,\ L_X\le X\le 1 \Rightarrow U=V=0\ ,\ \partial\theta/\partial Y=0 \end{array} \tag{28c}$$

$$\forall\, X,Y \mid Y=1,\ 0\le X\le 1 \ \Rightarrow U=V=0,\ \partial\theta/\partial Y=0 \tag{28d}$$

$$\forall\, X,Y \ \Big|\ Y=-\left(L_Y/L_X\right)\left(X-L_X\right) \Rightarrow U=V=0\ ,\ R_k\left.\frac{\partial\theta}{\partial N}\right|_s=\left.\frac{\partial\theta}{\partial N}\right|_b \tag{28e}$$

3.1. Stream function and entropy generation

The dimensionless form of the streamline equation can be written as:

$$\frac{\partial^2\Psi}{\partial X^2}+\frac{\partial^2\Psi}{\partial Y^2}=-\left(\frac{\partial V}{\partial X}-\frac{\partial U}{\partial Y}\right) \tag{29}$$

In addition, the non-dimensional entropy generation relation can be written as

$$S_T=S_\theta+S_\psi=\frac{k_b}{k_f}\left[\left(\frac{\partial\theta}{\partial X}\right)^2+\left(\frac{\partial\theta}{\partial Y}\right)^2\right] +\chi\frac{\mu_b}{\mu_f}\left(2\left(\frac{\partial U}{\partial X}\right)^2+2\left(\frac{\partial V}{\partial Y}\right)^2+\left(\frac{\partial U}{\partial Y}+\frac{\partial V}{\partial X}\right)^2\right) \tag{30}$$

χ in the above relation, is the irreversibility parameter which is defined as:

$$\chi=\frac{\mu_f T_0}{k_f}\left(\frac{\alpha_f}{H\left(T_h-T_c\right)}\right)^2 \tag{31}$$

4. Rate of heat transfer

The rates of local heat transfer enter the cavity from the hot wall are obtained using the relations given below:

$$Nu_{Y1}=-R_k\left(\frac{\partial\theta}{\partial X}\right)_{X=0,\ 0\le Y\le L_Y} \tag{32a}$$

$$Nu_{Y2}=-\frac{k_b}{k_f}\left(\frac{\partial\theta}{\partial Y}\right)_{X=0,\ L_Y\le Y\le 1} \tag{32b}$$

The overall heat transfer rate through the solid triangular block can also be written as follows:

$$Nu_t=\int_0^{L_Y}Nu_{Y1}\,dY+\int_{L_Y}^{1}Nu_{Y2}\,dX \tag{33}$$

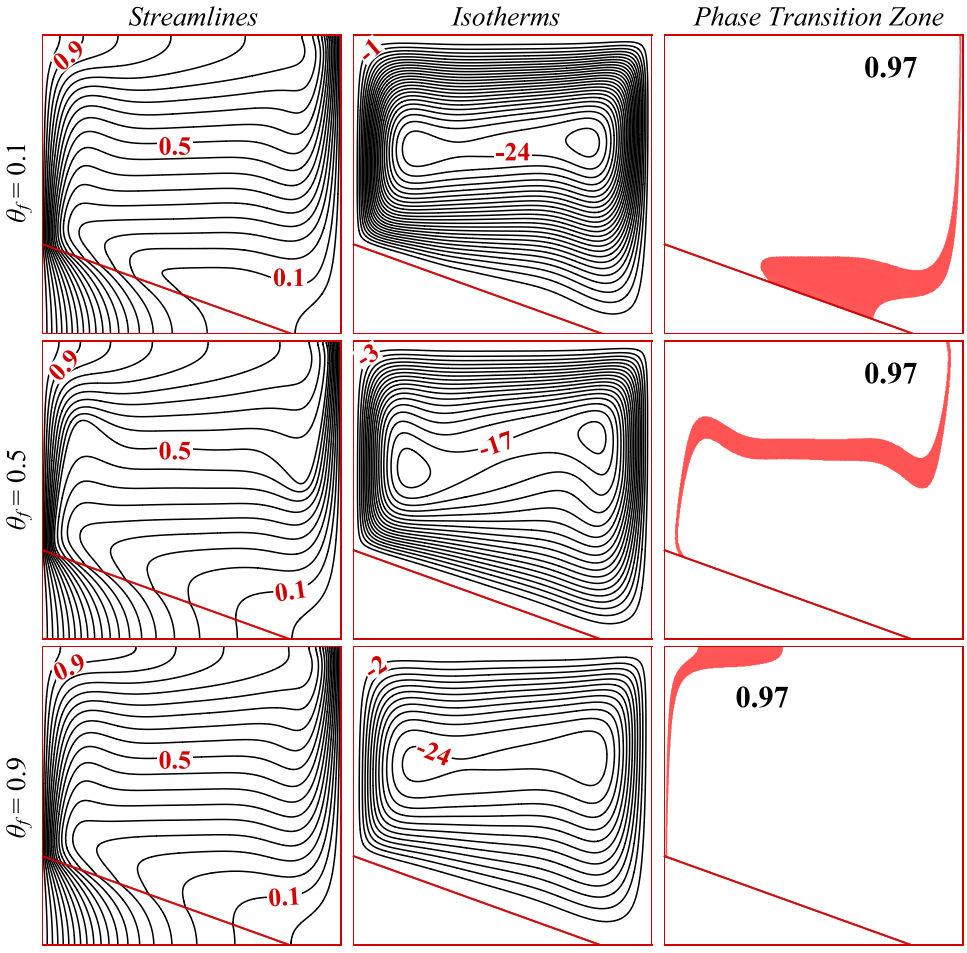

Fig. 8. Influence of the non-dimensional fusion temperature on the patterns of the isotherms, streamlines and the phase transition zone ($Ra = 10^6$, $R_k = 1$, $Ste = 0.2$, $\varphi = 0.05$, $L_Y = 0.3$).

5. Numerical approach and grid test

The non-dimensional governing equations subject to the boundary conditions (Eqs. (18)–20, 22, 27, and 28) were solved numerically using a weighted finite element method, named Galerkin's method. The discretization of the computational domain is done using a non-structured grid. It is noteworthy to mention that to capture the sharp variation of velocity and temperature near the solid walls, the generated grids in these areas are considered to be denser. The damped Newton method is applied to fully couple governing discretized equations. Finally, the solution for the corresponding linear algebraic equations is acquired using the Parallel Sparse Direct Solver. The computation is terminated when the residuals for all dependent variables become less than 10^{-5}. The used numerical method is described in detail in [40].

The grid check survey is conducted for the present study to guarantee a grid-independent solution. Five various non-uniform grid sizes are considered to select the appropriate grid size, as shown in Table 2, in which the relative errors are measured with respect to case 3. As a further analysis, the temperature profiles of the suspension along the vertical centerline of the cavity for the five cases are depicted in Fig. 2. The results obtained for the average Nusselt number at the hot vertical wall and the maximum velocity inside the cavity are presented for each grid size when $Ra = 10^6$, $R_k = 10$, $Pr = 6.2$, $Ste = 0.2$, $\theta_f = 0.1$, $\varphi = 0.05$, $Nc = 23.8$, $Nv = 12.5$, $\lambda = 0.333$, and $\delta = 0.05$. Consequently, by considering the computational cost and accuracy, the grid with 5520 elements (Case 3) has been selected for the following analysis.

The accuracy of the employed numerical code can be proved by comparing the current outcomes and those reported in [41–44]. Table 1 and Figs. 3 and 4 show these comparisons.

Table 3
Comparison between the results of the present study and Kahveci [41] ($Ra = 10^6$).

Nu_{avg}	$\varphi = 0.0$	$\varphi = 0.05$	$\varphi = 0.1$	$\varphi = 0.15$	$\varphi = 0.2$
Present study	9.20	9.76	10.30	10.80	11.20
Kahveci [41]	9.23	9.77	10.23	10.77	11.21

Table 3 compares the average Nusselt numbers of the present study and [41]. In [41], the buoyancy-driven convection of a suspension of water and TiO_2 nanoparticles in a clear square enclosure in which the side walls are isothermally heated and the horizontal walls are insulated.

As further verification, the temperature field of the developed numerical code for a simple fluid in a square medium enclosed has been compared with [42], as depicted in Fig. 3. Finally, the evaluated entropy fields of this work and those reported by [43] for a pure fluid are plotted in Fig. 4. It is worth mentioning that the boundary conditions of [42,43] are exactly the same as [41]. In the last validation, the temperature fields of the current numerical work and experimental study of Calcagni et al. [44] have been compared and depicted in Fig. 5 for $\varphi = 0$. It is worth noting that, In the experiments of [44], the enclosure when Rayleigh number is 1.836×10^5 and Prandtl number is 0.71. In this case, the vertical walls were adiabatic, the bottom wall was partially heated, and the upper wall was isothermally kept at a cold temperature of $\theta = 0$.

As clearly seen from the verifications, an admissible agreement can be found with the literature, specifying that the developed finite element code is accurate.

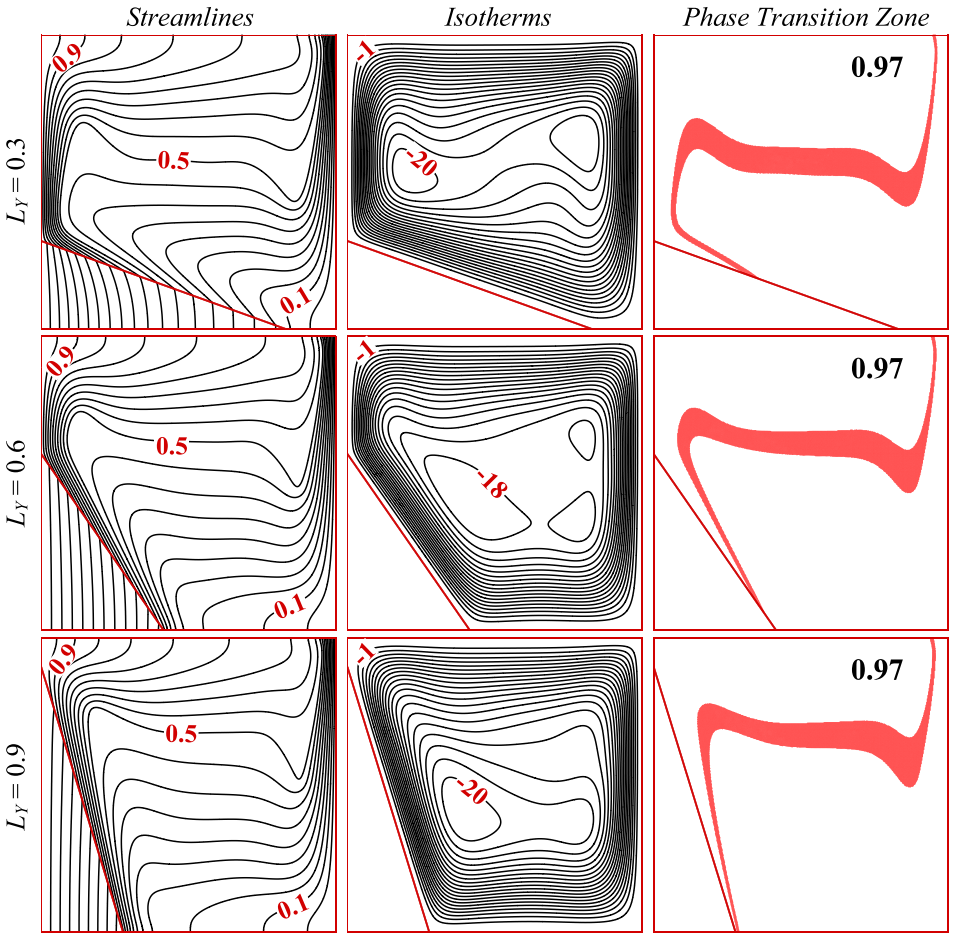

Fig. 9. Influence of the non-dimensional height of the solid triangular block on the patterns of the isotherms, streamlines and the phase transition zone ($Ra = 10^6$, $R_k = 10$, $Ste = 0.2$, $\theta_f = 0.5$, $\varphi = 0.05$).

6. Results and discussion

The conjugate natural convection flow and heat transport and the rate of generated entropy are assessed in the current work for an enclosure occupied with a suspension of water and dispersed NEPCMs particles. A solid triangular block with a constant area is attached to the bottom and left walls. In this work, the non-dimensional variables are Rayleigh number ($10^4 \leq Ra \leq 10^6$), Stefan number ($0.2 \leq Ste \leq 0.9$), non-dimensional fusion temperature ($0.05 \leq \theta_f \leq 0.95$), the non-dimensional height of the solid triangular block ($0.25 \leq L_Y \leq 0.95$), thermal conductivity ratio parameter ($1 \leq R_k \leq 10$), volume fraction of NEPCMs particles ($0.0 \leq \varphi \leq 0.05$). However, the other parameters are constant as $Pr = 6.2$, $Nv = 12.5$, $Nc = 23.8$, $\delta = 0.05$, $\lambda = 0.322$.

6.1. Heat and fluid flow analysis

Fig. 6 illustrates the influence of the Rayleigh number and thermal conductivity ratio on the streamlines, isotherms, and the phase transition zone of the suspension. As discussed before, the influence of the phase transition of the nano-capsules is reflected in their temperature-dependent heat capacity. According to Eq. (24), when the volume fraction of the NEPCMs particles is 0.05, the heat capacity ratio is constant and identical to 0.97 in the regions wherein the fluid temperature is below or above the melting point of the encapsulated PCM. The phase transition zone depicts the area in which the capsules are melted partially and thus forms and develops around the corresponding fluid isotherm, and the heat capacity ratio increases in this zone. The suspension is heated near the hot wall, resulting in a reduction in its density, and the induced buoyancy force drives the suspension vertically up near the hot wall and horizontally along the insulated top wall. The suspension then flows downward due to the imposed negative buoyancy force (as the suspension is cooled near the cold wall) and passes along the adiabatic bottom wall (and also the solid triangular block). Consequently, a clockwise vortex (circulation) is formed in the cavity. The formed vortex is, in fact, responsible for the advection mode of heat transfer in the cavity and conveys the nano-capsules with its motion. The red ribbon of the phase transition zone divides the cavity into two parts, the region near the hot wall wherein the PCMs of the capsules are completely melted, and the other one in the vicinity of the cold wall where the capsules are entirely solidified.

Three distinct phenomena of absorbing, storing, and releasing of the heat occur in the cores of the capsules. For the NEPCMs, the absorbing of the heat takes place when the circulating suspension enters the lower part of the Cr contour (where the fluid comprising solid NEPCMs flows from the cold wall and passes through the ribbon). The capsules store the absorbed heat throughout the region near the hot wall (where the temperature of the suspension is above the melting temperature of the PCM) and release it in the upper region of the ribbon (where the suspension of melted NEPCMs flows from the hot wall to the cold one). The Rayleigh number characterizes the buoyancy force, and therefore, its amplification intensifies the fluid flow and, consequently, the rate of heat transfer.

The isotherms for the case of $Ra = 10^4$ are almost vertical, indicating the dominance of the conduction mechanism, while their distortion for high Rayleigh number increases, specifying that the convection mode mainly governs the heat transfer. Increasing the Rayleigh number also affects the phase transition zone, and the ribbon of the phase transition zone widens, indicating that capsules of a larger region experience the phase change. Increasing the thermal conductivity of the solid matrix boosts the effective thermal conductivity of the cavity and intensifies

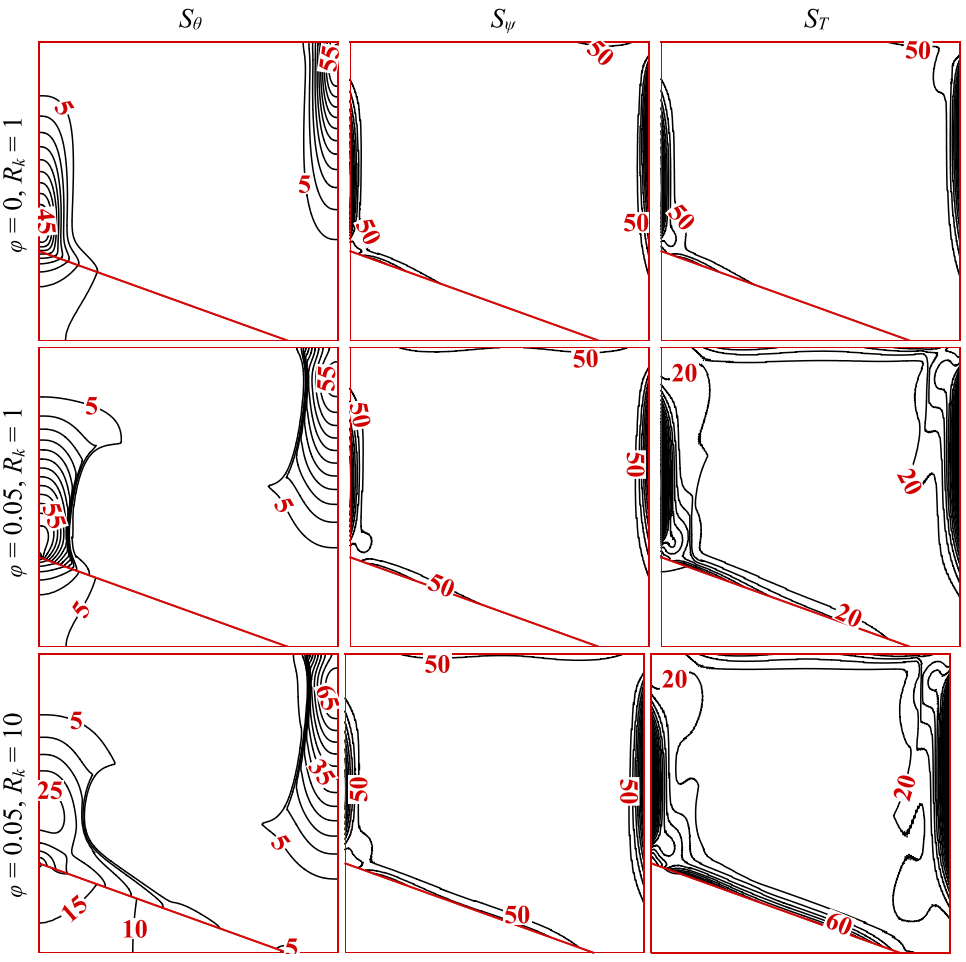

Fig. 10. Influence of the volume fraction of NEPCMs and the thermal conductivity of the solid block on the patterns of the thermal component of the local entropy generation (S_θ), local generated entropy caused by friction of the fluid (S_ψ) and the local generated entropy (S_T) ($Ra = 10^5$, $Ste = 0.2$, $\theta_f = 0.5$, $L_Y = 0.3$).

the conduction mechanism. As a result, the rate of heat transfer and also the fluid strength increases.

The dependency of the flow, thermal, and phase transition fields to the volume fraction of particles and the Stefan number are outlined in Fig. 7. Adding the nanoparticles of encapsulated phase change materials to the host fluid alters the suspension's thermophysical properties and also involves the latent heat of the PCMs. These impacts are separately illustrated and compared in Fig. 7. Indeed, the presence of the nano-capsules with very high Stefan number (i.e., with approximately zero latent heat) only increases the dynamic viscosity and the thermal conductivity of the suspension. The increment of the viscosity reduces the fluid flow in the cavity. The augmentation of the thermal conductivity elevates the rate of heat transfer and thus intensifies the natural convection and the strength of the induced vortex. In other words, the presence of the NEPCMs without considering their ability to store/release the heat intensifies the fluid flow. Reducing the Stefan number enables the absorbing/storing/releasing mechanisms of the PCMs in the nano-capsules.

As seen, for $Ste = 0.2$, the temperature isoline corresponding to the non-dimensional fusion temperature of the NEPCMs is distorted somewhat by adding the nano-capsules. In addition, in comparison with the case of $Ste \to \infty$, the fluid flow declines, and the isotherms slightly move to the sidewalls, indicating an augmentation of the heat transfer. By reducing the Stefan number, more energy, in the form of the latent heat, can be stored in the cores of the nano-capsules, and thus the rate of heat transfer augments. The decrease of the fluid flow can be attributed to the fact that the temperature of the suspension around its non-dimensional fusion temperature is almost constant, and therefore, the buoyancy force declines and reduces the fluid flow. Besides, the ribbon of the phase transition zone enlarges as the Stefan number declines, indicating that the phase change occurs in more capsules and in a wider area.

The influence of the non-dimensional fusion temperature on the patterns of the streamlines, isolines of the temperature, and the phase transition zone is shown in Fig. 8. As discussed before, the red ribbons specifying the phase transition zones are formed around the related isotherms. Moreover, in comparison with the other cases, the isotherms for the case of $\theta_f = 0.5$ move slightly toward the vertical walls, indicating an increment in the rate of transferred heat. This is reasonable by considering the mechanisms of absorbing and releasing heat for the cases of $\theta_f = 0.1$ and 0.9. When $\theta_f = 0.1$, the majority of the NEPCMs are in the state of liquid, and also the flow rate of suspension passing the phase transition zone is almost negligible. This means that minimal numbers of the capsules release their latent heat and solidify.

Similarly, for $\theta_f = 0.9$, in almost entire of the cavity, the capsules are completely melted, and few numbers of the capsules pass through the phase transition zone, and therefore, the absorbing heat and phase change is feeble. For the case of $\theta_f = 0.5$, both mechanisms contribute favorably and thus intensify the rate of heat transfer. In other words, it can be concluded that for the suspension comprising the NEPCMs, there should be a balance between the melted and solidified regions to achieve a higher rate of heat transfer. The streamline contours exhibit a slight decline in the fluid strength when $\theta_f = 0.5$, which can be described by the fact that for this case, the latent heat of the PCMs plays a more significant role than the other cases. As discussed before, the higher stored heat in the capsules results in lower fluid flow as it decreases the liquid temperature and buoyancy force.

Fig. 9 depicts the impact of the non-dimensional height of the solid triangular block on the streamlines, isotherms, and the phase transition

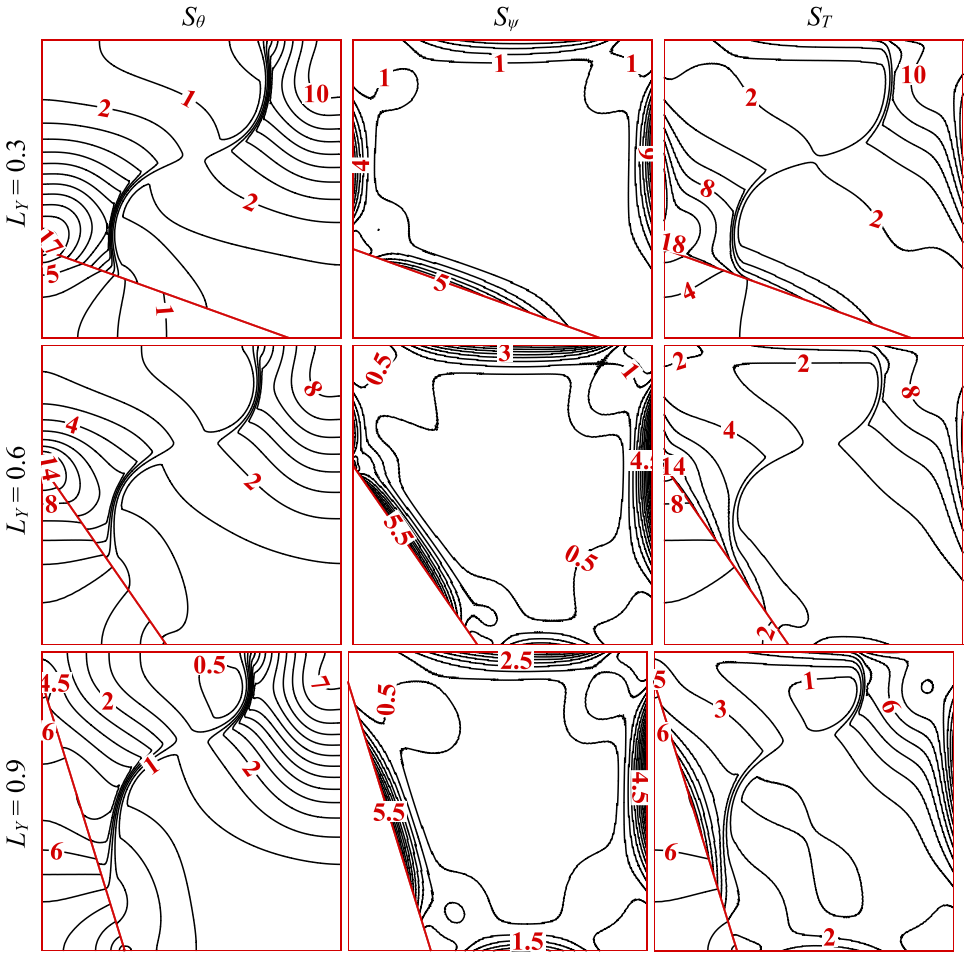

Fig. 11. Influence of the non-dimensional height of the solid triangular block on the patterns of the thermal component of the local entropy generation (S_θ), local generated entropy caused by friction of the fluid (S_ψ) and the local generated entropy (S_T ($Ra = 10^4$, $R_k = 1$, $Ste = 0.2$, $\theta_f = 0.5$, $\varphi = 0.05$).

zone. As specified before, the surface area of the solid triangular block is considered to be constant, and thus by increasing L_Y, the L_X should be decreased. The pattern of the transferred heat changes with increasing the L_Y. In fact, the direction of the conducted heat from the triangular block to the suspension alters from vertical heating to the horizontal one. According to the streamlines, the fluid flow intensifies in the vicinity of the solid triangular wall as L_Y increases, and the fluid flow is minimum when the $L_Y = 0.6$.

6.2. Entropy generation

Fig. 10 depicts the dependency of the local entropy generation (S_T) to the volume fraction of the nanoparticles and the thermal conductivity of the triangular block. In this figure, the two components of entropy generation, which are the heat transfer (S_θ) and the friction of the fluid flow (S_θ), are investigated. The isolines of the S_θ are mainly concentrated near the lower part of the hot wall and upper portion of the cold one, representing the dominant regions of the heat transfer irreversibilities.

It can be observed that the generated entropy induced by heat transfer is strongly affected by adding the NEPCMs. The isotherms and thus the isolines of the S_θ distort around the melting region of the nanocapsules when the nanoparticles are added to the base fluid. Moreover, the intensification of the R_k augments the entropy generation induced by heat transfer. In contrast with the S_θ, the influence of the discussed parameters on the fluid friction irreversibilities is negligible as these parameters slightly alter the flow field. Finally, the local entropy generation intensifies with an increment of the φ and R_k and spreads throughout the cavity as its heat transfer component amplifies.

Influence of the non-dimensional height of the solid triangular block on the patterns of the thermal component of the local entropy generation (S_θ), local generated entropy caused by friction of the fluid (S_ψ), and the local generated entropy (S_T) is outlined in Fig. 11. By increasing the L_Y, the entropy generation caused by heat transfer decreases, specifying that the rate of transferred heat is reduced. The direction of the heat transfer is from solid to the suspension, which is changed from vertical heating to horizontal one by increasing the L_Y. The fluid friction portion of the generated entropy slightly increases, and the local entropy generation (S_T) decreases with the increment of the non-dimensional height of the solid triangular block.

Fig. 12 outlines the influence of the non-dimensional fusion temperature on the thermal component of the local entropy generation (S_θ), local generated entropy caused by friction of the fluid (S_ψ), and the local generated entropy (S_T). It is evident that the isolines of S_θ distort around the corresponding isotherms (See Fig. 8) due to the change in the heat capacity of suspension in the phase transition zone. As discussed before, the fluid strength declines, and the rate of heat transfer intensifies as when the non-dimensional fusion temperature is 0.5. Therefore, when $\theta_f = 0.5$, the local entropy generation due to heat transfer amplifies, and the S_ψ declines. As a result, the entropy generation for this case is maximum. In addition, it can be found that for the cases of $\theta_f = 0.1$ and 0.9, the patterns of the local entropy generation induced by the friction of the fluid are quite similar.

6.3. Rates of transferred heat and generated entropy

Fig. 13 shows the dependency of the average Nusselt number and the total entropy generation to the non-dimensional fusion temperature, Stefan number, and the thermal conductivity of the solid triangu-

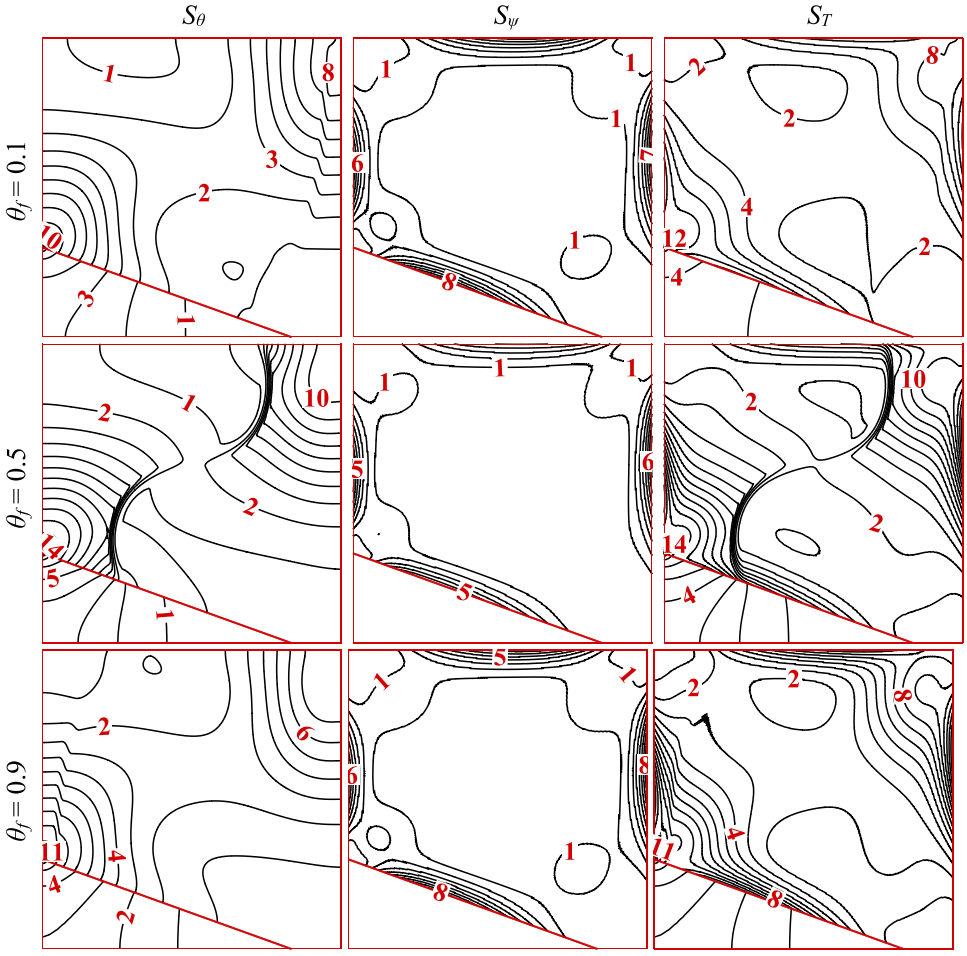

Fig. 12. Influence of the non-dimensional fusion temperature of the NEPCMs on the patterns of the thermal component of the local entropy generation (S_θ), local generated entropy caused by friction of the fluid (S_ψ) and the local generated entropy (S_T) ($Ra = 10^4$, $R_k = 1$, $Ste = 0.2$, $\theta_f = 0.5$, $\varphi = 0.05$).

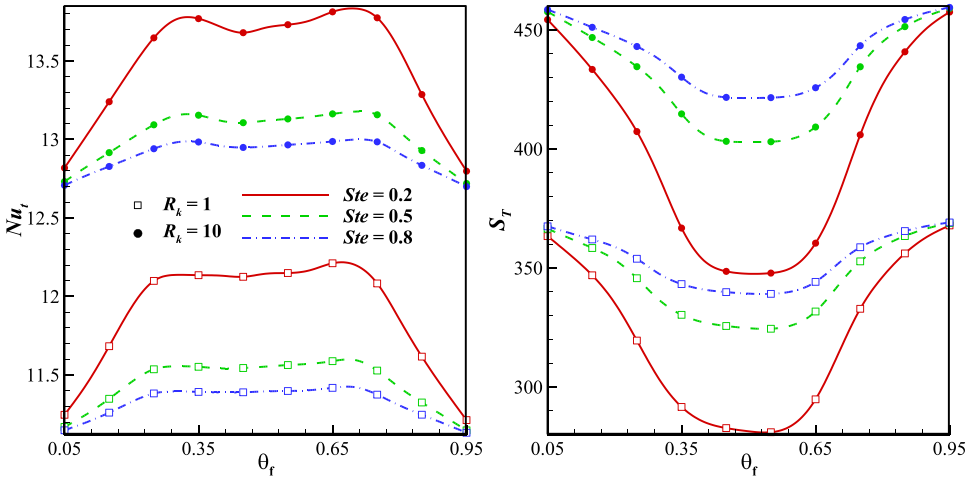

Fig. 13. Variation of the average Nusselt number and total entropy generation with the R_k, Stefan number and the non-dimensional fusion temperature of the NEPCMs ($Ra = 10^6$, $\varphi = 0.05$, $L_Y = 0.3$).

lar block. It is evident that the rate of heat transfer intensifies when the non-dimensional fusion temperature varies between 0.3 and 0.6. In fact, when $0.3 \leq \theta_f \leq 0.6$, the absorbing and releasing mechanisms are engaged more effectively, resulting in the amplification of the transferred heat. The Stefan number characterizes the latent heat of the NEPCMs, and thus its decrease intensifies the rate of heat transfer. The increment of the triangular block's thermal conductivity boosts the heat conduction in the cavity and thus augments the Nu_t. The total entropy generation declines, as the non-dimensional fusion temperature approaches 0.5, since the heat transfer intensifies, and the fluid flow decays.

For $Ra = 10^6$, shown in Fig. 13, the reduction of the S_ψ overtakes the increment of the $S_{\theta,}$ and thus the total entropy generation declines as $\theta_f \rightarrow 0.5$. In contrast, when $Ra = 10^4$, as depicted in Fig. 12, the increase of the heat transfer irreversibilities is adequate to compensate for the reduction of the entropy generation induced by the fluid friction, and thus the total generated entropy elevates for this case. Similarly, the S_T raises with the increment of the *Ste*, since, as shown in Fig. 7, the heat transfer declines, and the fluid flow elevate. Finally, due to the increment of the heat transfer with increasing the R_k, the total entropy generation intensifies.

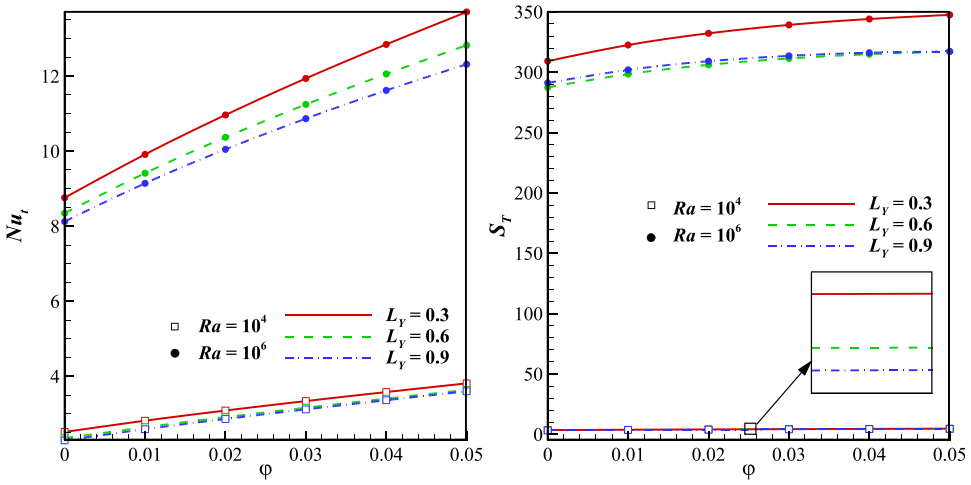

Fig. 14. Variation of the average Nusselt number and total entropy generation with the non-dimensional height of the solid triangular block, the volume fraction of the NEPCMs and the Rayleigh number (R_k = 10, Ste = 0.2, θ_f = 0.5).

Variation of the average Nusselt number and total entropy generation with the L_Y, φ, and the Rayleigh number is depicted in Fig. 14. It is evident that the Nusselt number linearly increases with the increment of the nano-capsules volume fraction as the thermal conductivity of the suspension augments, and also, a higher amount of the latent heat is absorbed and released. The Rayleigh number represents the buoyancy force, and thus, its increase intensifies the rate of heat transfer. The Nusselt number declines as the non-dimensional height of the solid triangular block increases. The figure for the total generated entropy boosts as the φ rises. This indicates that the increment rate of the S_θ is higher than the reduction rate of S_ψ. Furthermore, raising the L_Y reduces the rate of entropy generation. Besides, for $Ra = 10^6$, the S_T for $L_Y = 0.9$ is higher than the case of $L_Y = 0.6$ for pure fluid or when the volume fraction of the NEPCMs is low, and their entropy generation coincides when φ approaches 5%.

7. Conclusion

Natural laminar convective heat transfer and entropy generation of a homogeneous suspension containing nano-encapsulated phase change materials inside a square cavity is numerically analyzed using the Galerkin Finite Element Method. A solid triangular block is attached to the left-bottom of the cavity, the side walls are subjected to a temperature difference, and the top and bottom walls are well insulated. The phase transition of the nano-capsules is addressed as an increase in the local heat capacity of the suspension, resulting in a temperature-dependent heat capacity field. The heat capacity field represents the zone in which the phase transition occurs in the core of the capsules. Influence of the key parameters on the patterns streamlines, isotherms, the contour of the phase transition zone, the local entropy generation as well as the average Nusselt number and the total entropy generation is studied, and the outcome of this study can be summarized as follow:

1 The fluid strength and the rate of heat transfer intensify with the augmentation of the Rayleigh number and also the thermal conductivity of the triangular block.
2 Adding the NEPCMs to the host fluid increases the viscosity and thermal conductivity of the suspension and also entails the latent heat of the PCMs. The fluid flow and the rate of heat transfer amplify as a result of the alteration of the suspension's thermophysical properties. Besides, reducing the Stefan number intensifies the rate of heat transfer and also reduces the fluid flow in the cavity.
3 The rate of heat transfer intensifies, and the fluid strength diminishes as the non-dimensional fusion temperature approaches 0.5.
4 The isolines of the S_θ are mainly concentrated near the lower part of the hot wall and upper portion of the cold one, showing the dominant regions of the heat transfer irreversibility. The generated entropy induced by heat transfer is strongly affected by adding the NEPCMs. Moreover, the isolines of the S_θ distort around the melting region of the nano-capsules.
5 The influence of the volume fraction of the nanoparticles and the thermal conductivity of the triangular block on the fluid friction irreversibility is negligible as these parameters alter the flow field very slightly.
6 By increasing the L_Y, the entropy generation caused by heat transfer decreases, specifying that the rate of transferred heat is reduced. Moreover, the fluid friction portion of the generated entropy slightly increases with the increment of the non-dimensional height of the solid triangular block.
7 When the non-dimensional fusion temperature approaches 0.5, the thermal component of the local entropy generation amplifies, and the S_ψ declines. Besides, the patterns of the local generated entropy induced by the friction of the fluid are quite similar for the cases of θ_f = 0.1 and 0.9.
8 The average Nusselt number elevates as the non-dimensional fusion temperature varies between 0.3 and 0.6. Moreover, the increment of the triangular block's thermal conductivity boosts the heat conduction in the cavity and thus augments the Nu_t.
9 For high values of the Rayleigh number ($Ra = 10^6$), the total entropy generation declines as the non-dimensional fusion temperature approaches 0.5. In contrast, when the buoyancy force is low, the total entropy generation elevates as $\theta_f \to 0.5$.
10 The Nusselt number linearly increases with the increment of the nano-capsules volume fraction. Moreover, the Nu_t decreases as the non-dimensional height of the solid triangular block increases
11 The total entropy generation enhances and decreases with the increment of the volume fraction of the NEPCMs and the non-dimensional height of the solid triangular block, respectively.

Declaration of Competing Interest

The authors clarify that there is no conflict of interest for report.

CRediT authorship contribution statement

Seyed Mohsen Hashem Zadeh: Conceptualization, Methodology, Software, Validation, Formal analysis, Data curation. **S.A.M. Mehryan:** Visualization, Writing - original draft, Investigation, Formal analysis, Data curation. **Mikhail Sheremet:** Investigation, Writing - review & editing. **Maryam Ghodrat:** Conceptualization, Investigation, Supervision, Writing - review & editing. **Mohammad Ghalambaz:** Conceptualization, Methodology, Validation, Writing - original draft, Supervision, Writing - review & editing.

References

[1] Shamberger PJ, Bruno NM. Review of metallic phase change materials for high heat flux transient thermal management applications. Appl Energy 2020;258:113955.

[2] Li S-F, Liu Z-h, Wang X-J. A comprehensive review on positive cold energy storage technologies and applications in air conditioning with phase change materials. Appl Energy 2019;255:113667.

[3] Leong KY, Abdul Rahman MR, Gurunathan BA. Nano-enhanced phase change materials: a review of thermo-physical properties, applications and challenges. J Energy Storage 2019;21:18–31.

[4] Alehosseini E, Jafari SM. Micro/nano-encapsulated phase change materials (PCMs) as emerging materials for the food industry. Trends Food Sci Technol 2019;91:116–28.

[5] Liu Z, Yu Z, Yang T, Qin D, Li S, Zhang G, Haghighat F, Joybari MM. A review on macro-encapsulated phase change material for building envelope applications. Build Environ 2018;144:281–94.

[6] Huo J-h, Peng Z-g, Xu K, Feng Q, Xu D-y. Novel micro-encapsulated phase change materials with low melting point slurry: characterization and cementing application. Energy 2019;186:115920.

[7] Kumirai T, Dirker J, Meyer J. Experimental analysis for thermal storage performance of three types of plate encapsulated phase change materials in air heat exchangers for ventilation applications. J Build Eng 2019;22:75–89.

[8] Bhagat K, Saha SK. Numerical analysis of latent heat thermal energy storage using encapsulated phase change material for solar thermal power plant. Renew Energy 2016;95:323–36.

[9] Li W, Chen W. Numerical analysis on the thermal performance of a novel PCM-encapsulated porous heat storage Trombe-wall system. Solar Energy 2019;188:706–719.

[10] Caliano M, Bianco N, Graditi G, Mongibello L. Analysis of a phase change material-based unit and of an aluminum foam/phase change material composite-based unit for cold thermal energy storage by numerical simulation. Appl Energy 2019;256:113921.

[11] Praveen B, Suresh S, Pethurajan V. Heat transfer performance of graphene nano–platelets laden micro-encapsulated PCM with polymer shell for thermal energy storage based heat sink. Appl Therm Eng 2019;156:237–49.

[12] Rao Z, Wang S, Peng F. Molecular dynamics simulations of nano-encapsulated and nanoparticle-enhanced thermal energy storage phase change materials. Int J Heat Mass Transf 2013;66:575–84.

[13] Ghalambaz M, Groşan T, Pop I. Mixed convection boundary layer flow and heat transfer over a vertical plate embedded in a porous medium filled with a suspension of nano-encapsulated phase change materials. J Mol Liq 2019;293:111432.

[14] Ghalambaz M, Chamkha AJ, Wen D. Natural convective flow and heat transfer of nano-encapsulated phase change materials (NEPCMs) in a cavity. Int J Heat Mass Transf 2019;138:738–49.

[15] Hajjar A, Mehryan S, Ghalambaz M. Time periodic natural convection heat transfer in a nano-encapsulated phase-change suspension. Int J Mech Sci 2020;166:105243.

[16] Li W, Zhang D, Jing T, Gao M, Liu P, He G, Qin F. Nano-encapsulated phase change material slurry (Nano-PCMS) saturated in metal foam: a new stable and efficient strategy for passive thermal management. Energy 2018;165:743–51.

[17] Tumirah K, Hussein M, Zulkarnain Z, Rafeadah R. Nano-encapsulated organic phase change material based on copolymer nanocomposites for thermal energy storage. Energy 2014;66:881–90.

[18] Rashidi S, Akar S, Bovand M, Ellahi R. Volume of fluid model to simulate the nanofluid flow and entropy generation in a single slope solar still. Renew Energy 2018;115:400–10.

[19] Sheikholeslami M, Ashorynejad H, Rana P. Lattice Boltzmann simulation of nanofluid heat transfer enhancement and entropy generation. J Mol Liq 2016;214:86–95.

[20] Sheremet MA, Oztop HF, Pop I, Abu-Hamdeh N. Analysis of entropy generation in natural convection of nanofluid inside a square cavity having hot solid block: Tiwari and Das' model. Entropy 2016;18:9.

[21] Bondareva NS, Sheremet MA, Oztop HF, Abu-Hamdeh N. Entropy generation due to natural convection of a nanofluid in a partially open triangular cavity. Adv Powder Technol 2017;28:244–55.

[22] Selimefendigil F, Öztop HF. Effects of conductive curved partition and magnetic field on natural convection and entropy generation in an inclined cavity filled with nanofluid. Physica A 2020;540:123004.

[23] Alsabery AI, Gedik E, Chamkha AJ, Hashim I. Impacts of heated rotating inner cylinder and two-phase nanofluid model on entropy generation and mixed convection in a square cavity. Heat Mass Transf 2020;56:321–38.

[24] Mansour M, Armaghani T, Chamkha A, Rashad A. Entropy generation and nanofluid mixed convection in a C-shaped cavity with heat corner and inclined magnetic field. Eur Phys J Spec Top 2019;228:2619–45.

[25] Alsabery A, Selimefendigil F, Hashim I, Chamkha A, Ghalambaz M. Fluid-structure interaction analysis of entropy generation and mixed convection inside a cavity with flexible right wall and heated rotating cylinder. Int J Heat Mass Transf 2019;140:331–45.

[26] Rashad A, Armaghani T, Chamkha AJ, Mansour M. Entropy generation and MHD natural convection of a nanofluid in an inclined square porous cavity: effects of a heat sink and source size and location. Chin J Phys 2018;56:193–211.

[27] Ishak MS, Alsabery AI, Chamkha A, Hashim I. Effect of finite wall thickness on entropy generation and natural convection in a nanofluid-filled partially heated square cavity. Int J Numer Methods Heat Fluid Flow 2019;30(3):1518–46.

[28] Alsabery A, Mohebbi R, Chamkha A, Hashim I. Impacts of magnetic field and non-homogeneous nanofluid model on convective heat transfer and entropy generation in a cavity with heated trapezoidal body. J Therm Anal Calorim 2019;138:1371–94.

[29] Tayebi T, Chamkha AJ. Entropy generation analysis due to MHD natural convection flow in a cavity occupied with hybrid nanofluid and equipped with a conducting hollow cylinder. J Therm Anal Calorim 2020;139:2165–79.

[30] Tayebi T, Chamkha AJ. Entropy generation analysis during MHD natural convection flow of hybrid nanofluid in a square cavity containing a corrugated conducting block. Int J Numer Methods Heat Fluid Flow 2019;30(3):1115–36.

[31] Barlak S, Sara ON, Karaipekli A, Yapıcı S. Thermal conductivity and viscosity of nanofluids having nanoencapsulated phase change material. Nanoscale Microscale Thermophys Eng 2016;20:85–96.

[32] Ghalambaz M, Sheremet MA, Pop I. Free convection in a parallelogrammic porous cavity filled with a nanofluid using Tiwari and Das' nanofluid model. PLoS ONE 2015;10:e0126486.

[33] Chai L, Shaukat R, Wang L, Wang HS. A review on heat transfer and hydrodynamic characteristics of nano/microencapsulated phase change slurry (N/MPCS) in mini/microchannel heat sinks. Appl Therm Eng 2018;135:334–49.

[34] Chen B, Wang X, Zeng R, Zhang Y, Wang X, Niu J, Li Y, Di H. An experimental study of convective heat transfer with microencapsulated phase change material suspension: laminar flow in a circular tube under constant heat flux. Exp Therm Fluid Sci 2008;32:1638–46.

[35] Khanafer K, Vafai K. A critical synthesis of thermophysical characteristics of nanofluids. Int J Heat Mass Transf 2011;54:4410–28.

[36] Seyf HR, Zhou Z, Ma H, Zhang Y. Three dimensional numerical study of heat-transfer enhancement by nano-encapsulated phase change material slurry in microtube heat sinks with tangential impingement. Int J Heat Mass Transf 2013;56:561–73.

[37] Zaraki A, Ghalambaz M, Chamkha AJ, Ghalambaz M, De Rossi D. Theoretical analysis of natural convection boundary layer heat and mass transfer of nanofluids: effects of size, shape and type of nanoparticles, type of base fluid and working temperature. Adv Powder Technol 2015;26:935–46.

[38] Ghalambaz M, Doostani A, Izadpanahi E, Chamkha AJ. Phase-change heat transfer in a cavity heated from below: the effect of utilizing single or hybrid nanoparticles as additives. J Taiwan Inst Chem Eng 2017;72:104–15.

[39] Selimefendigil F, Öztop HF, Chamkha AJ. MHD mixed convection and entropy generation of nanofluid filled lid driven cavity under the influence of inclined magnetic fields imposed to its upper and lower diagonal triangular domains. J Magn Magn Mater 2016;406:266–81.

[40] . The finite element method for fluid dynamics. In: Zienkiewicz OC, Taylor RL, Nithiarasu P, editors. The finite element method for fluid dynamics. Oxford: Butterworth-Heinemann; 2014. iii.

[41] Kahveci K. Buoyancy driven heat transfer of nanofluids in a tilted enclosure. J Heat Transfer 2010;132:062501.

[42] Turan O, Sachdeva A, Chakraborty N, Poole RJ. Laminar natural convection of power-law fluids in a square enclosure with differentially heated side walls subjected to constant temperatures. J Nonnewton Fluid Mech 2011;166:1049–63.

[43] Ilis GG, Mobedi M, Sunden B. Effect of aspect ratio on entropy generation in a rectangular cavity with differentially heated vertical walls. Int Commun Heat Mass Transf 2008;35:696–703.

[44] Calcagni B, Marsili F, Paroncini M. Natural convective heat transfer in square enclosures heated from below. Appl Therm Eng 2005;25:2522–31.